OPTICA

Entanglement generation using cryogenic integrated four-wave mixing

Lan-Tian Feng,[1,2,3,†] Yu-Jie Cheng,[1,2,3,†] Xiao-Zhuo Qi,[1,2,3] Zhi-Yuan Zhou,[1,2,3] Ming Zhang,[4] Dao-Xin Dai,[4] Guang-Can Guo,[1,2,3] and Xi-Feng Ren[1,2,3,*]

[1]CAS Key Laboratory of Quantum Information, University of Science and Technology of China, Hefei 230026, China
[2]CAS Synergetic Innovation Center of Quantum Information & Quantum Physics, University of Science and Technology of China, Hefei 230026, China
[3]Hefei National Laboratory, University of Science and Technology of China, Hefei 230088, China
[4]State Key Laboratory for Modern Optical Instrumentation, Centre for Optical and Electromagnetic Research, Zhejiang Provincial Key Laboratory for Sensing Technologies, Zhejiang University, Zijingang Campus, Hangzhou 310058, China
[†]These authors contributed equally to this work.
*renxf@ustc.edu.cn

Received 26 September 2022; revised 6 May 2023; accepted 10 May 2023; published 2 June 2023

Cryogenic integrated nonlinear photonics can provide fundamental building blocks for scalable photonic quantum computing and optical interfacing among different platforms. Here, we investigate the spontaneous four-wave mixing effect in an integrated silicon waveguide with cryogenic operating conditions (4 K) and employ the system to generate the entangled photon-pair source, one of the key elements of photonic quantum information applications. We experimentally prove that even at cryogenic temperatures, the four-wave mixing effect in silicon waveguides is still an effective method to generate quantum photonic sources. The cryogenic photon-pair source is verified over multiple frequency channels within a bandwidth of ∼2 THz. Furthermore, the source is used to generate high-quality frequency-multiplexed energy–time entangled states. Our results will advance the development of cryogenic nonlinear photonics and scalable integrated photonics for quantum information processing.

https://doi.org/10.1364/OPTICA.476712

1. INTRODUCTION

Photonic integrated circuits (PICs) have developed into a compelling platform to providing fundamental building blocks for a wide range of quantum information applications [1]. By using optical waveguides to guide and route photons, this technology provides phase-stable circuitry with millimeter-scale footprints for different quantum core functionalities, such as nonclassical photonic quantum sources [2–5], programmable photonic quantum processors [6–11], and single-photon detectors [12–14]. Furthermore, because photons can be transmitted over a long distance via optical fiber and are thus essential for constructing quantum networks [15], quantum PICs (QPICs) are becoming a possible candidate to interface different quantum systems with hybrid integrated techniques [16].

Until now, most investigations on QPICs have focused on operation at ambient temperatures; however, many quantum components, such as superconducting nanowire single-photon detectors (SNSPDs) [12,13], as well as semiconducting and superconducting quantum computing systems [17,18], have to operate under cryogenic conditions. For scalable photonic quantum computing and interfacing among different quantum systems, quantum technologies must be mutually compatible. Therefore, QPICs that are optimized to operate at room temperature, in particular, those involving nonlinear processes, should be extended to cryogenic environments [19].

The four-wave mixing effect in integrated waveguides is widely used in a variety of nonlinear processes and has great prospects in all-optical signal processing for classical and quantum applications. For example, combined with the four-wave mixing effect, silicon photonics provides a versatile test bed for quantum photonics and plays an important role in scalable photonic quantum information applications [20]. This nonlinear effect can generate new frequencies and effectively realize different functions in various configurations, such as wavelength conversion and parametric amplification [21–23], heralded single photons [24–26], two-photon and multi-photon entangled states [27–32], and squeezed states [5,33,34]. Demonstrating this capability under cryogenic operating conditions will undoubtedly expand the application scope of PICs.

In this paper, we investigate the spontaneous four-wave mixing (SFWM) effect in an integrated silicon waveguide under cryogenic operation conditions (4 K). We experimentally prove that SFWM in silicon waveguides is still an effective method to generate quantum photonic sources at cryogenic temperatures. Cryogenic photon pairs were generated and experimentally verified with a bandwidth of ∼2 THz, and noise generated in the photon-pair source preparation was carefully analyzed.

Furthermore, by feeding correlated photon pairs into a common unbalanced Michelson interferometer (UMI, 1.6 ns time difference), frequency-multiplexed energy–time entangled states were generated and analyzed. Near-unity raw interference visibilities were observed for multi-channel pairs, indicating the high quality of the cryogenic source. Our results represent an important part of cryogenic nonlinear photonics and will be further used in integrated scalable quantum information applications.

2. EXPERIMENTAL SETUP AND RESULTS

A. Experimental Setup

In the experiment, a continuous-wave (CW) laser (Santec, central wavelength 1550.12 nm) was used as the pump source. As shown in Fig. 1, the pump first passed through two cascaded 100 GHz bandwidth fiber pre-filters (filter 1, 100 dB extinction ratio) to remove the background noise. Then, it was coupled into the silicon device by a single-mode fiber array in a closed-cycle cryostat (Montana Instruments). A fiber polarization controller was placed between the filter and cryostat to adjust the polarization of the pump in the silicon waveguide, which was kept in TE_0 mode in the experiment. The silicon waveguide is 1.2 cm long with a cross section of $500 \times 220\ \text{nm}^2$, which satisfies the near-zero phase matching condition for SFWM. The generated signal–idler photons were input into a 40-channel dense-wave-division multiplexer (DWDM) to separate the signal and idler photons. Each DWDM frequency channel has a 100 GHz bandwidth, such that we can select multiplexed frequency combinations for photon pairs with a frequency detuning of ∼2 THz from the central pump frequency. The central wavelength of each DWDM channel and correspondence between the index of signal–idler channels (±1−±19) and international telecommunication union grids (C15–C53) are given in Table S1. Before the DWDM, we used two cascaded off-chip 200 GHz bandwidth fiber post-filters (filter 2, 100 dB extinction ratio) to block the pump light. The generated photon pairs were detected by two SNSPDs, which have dark count rates of approximately 100 Hz. Finally, the acquired electrical signals were collected and analyzed through the time-correlated single-photon counting system.

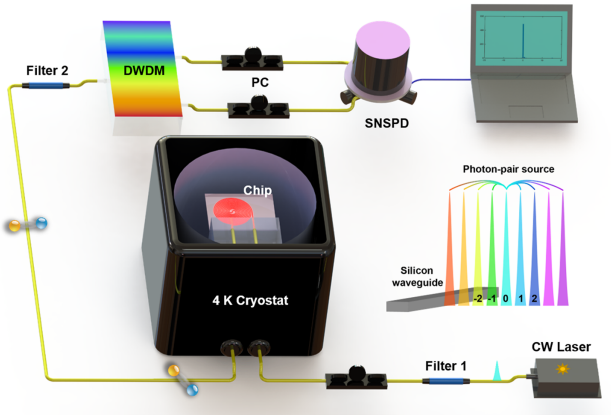

Fig. 1. Experimental setup. The integrated silicon waveguide and fiber array are placed in the closed-cycle cryostat. The fiber array and two on-chip end couplers are used for coupling the input pump and output signal–idler photons. Inset: frequency-multiplexed photon-pair generation using the silicon waveguide. CW Laser, continuous-wave laser; PC, polarization controller; DWDM, dense-wave-division multiplexer; SNSPD, superconducting nanowire single-photon detector.

B. Photon-Pair Source Characterization

By adjusting the temperature of the cryostat, we first recorded photon-pair production at 4 K and 294 K (i.e., room temperature) with 2 mW pump power (off-chip), and the experimental results are shown in Fig. 2. Note that the 294 K results are only for comparative analysis. With the pump wavelength as the center, the frequencies of the correlated photon pairs were equally separated. The DWDM system gives 38-channel single-photon counts (N_s and N_i, where s represents the signal and i represents the idler) and 19 photon-pair coincidence values (C_{exp}). By comparing the emission spectra at different temperatures [Figs. 2(a) and 2(d)], we found that the emission at 4 K was reduced, especially for channels close to the pump. Specifically, the photon flux decreased by 65% on average at frequencies lower than that of the pump and 68% on average at frequencies higher than that of the pump. As we know, this emission reduction has two main causes: one is SFWM reduction under cryogenic conditions, which is due to the attenuation of optical Kerr nonlinearity in the silicon waveguides [35], and the other is the noise suppression caused by cryogenic cooling [36]. The coincidence values for different channels are shown in Figs. 2(b) and 2(e). We can see that even at cryogenic temperatures, two-photon coincidence covers all channels, and SFWM in silicon waveguides is still an efficient method to prepare parametric quantum photonic sources. The brightness reduction is due to the attenuation of the optical Kerr nonlinearity in the silicon waveguides. Owing to the difference in efficiency with signal–idler channels in post-filtering and DWDM systems (see Table S1), we have normalized both the single channel and coincidence results here. The fluctuation in the emission spectra and coincidence results of different channels stems from the discrepancy in channel bandwidth, unfiltered laser noise, and fluctuation in coupling efficiency during the test. On average, the detected source brightness at 4 K was 41% lower than that at room temperature, which corresponds to a reduction in the Kerr nonlinear coefficient of approximately 23%. This value is consistent with the results in Ref. [35], which discussed the effect of temperature on optical nonlinear parameters in detail. Compared to coincidence counts, single-photon counts drop even more at 4 K, which is mainly caused by noise suppression resulting from cryogenic cooling. The ratio of the net coincidence value C_{net} and accident coincidence event A (CAR) is one key parameter for characterizing photon-pair sources. Using the formula $\text{CAR} = C_{\text{net}}/A$, we calculated the CAR values of different signal–idler channels at 4 and 294 K. In the formula, $C_{\text{net}} = C_{\text{exp}} - A$ and $A = N_s N_i t_{\text{win}} t_{\text{int}}$, where t_{int} is the coincidence integral time and t_{win} is the coincidence window. The results are shown in Figs. 2(c) and 2(f), respectively, and the CAR values improved at 4 K compared to those at 294 K. It is particularly noteworthy that at the channels close to the pump frequency, such as signal–idler channels ±2, the CAR exceeded 500:1, whereas in the room temperature case, it was less than 23:1. This CAR improvement enables more frequency channels to be used for further quantum information applications. In addition, because of noise suppression, a higher heralding efficiency can be achieved with this cryogenic photon-pair source (see Supplement 1). To explain the pattern of CAR in more detail, we further split the single-photon count into SFWM signals and noise. The CAR of the photon-pair source can be described as

$$\text{CAR} = \frac{G\eta_s\eta_i}{t_{\text{win}}[\eta_s(G+n_s)+D_s][\eta_i(G+n_i)+D_i]}, \quad (1)$$

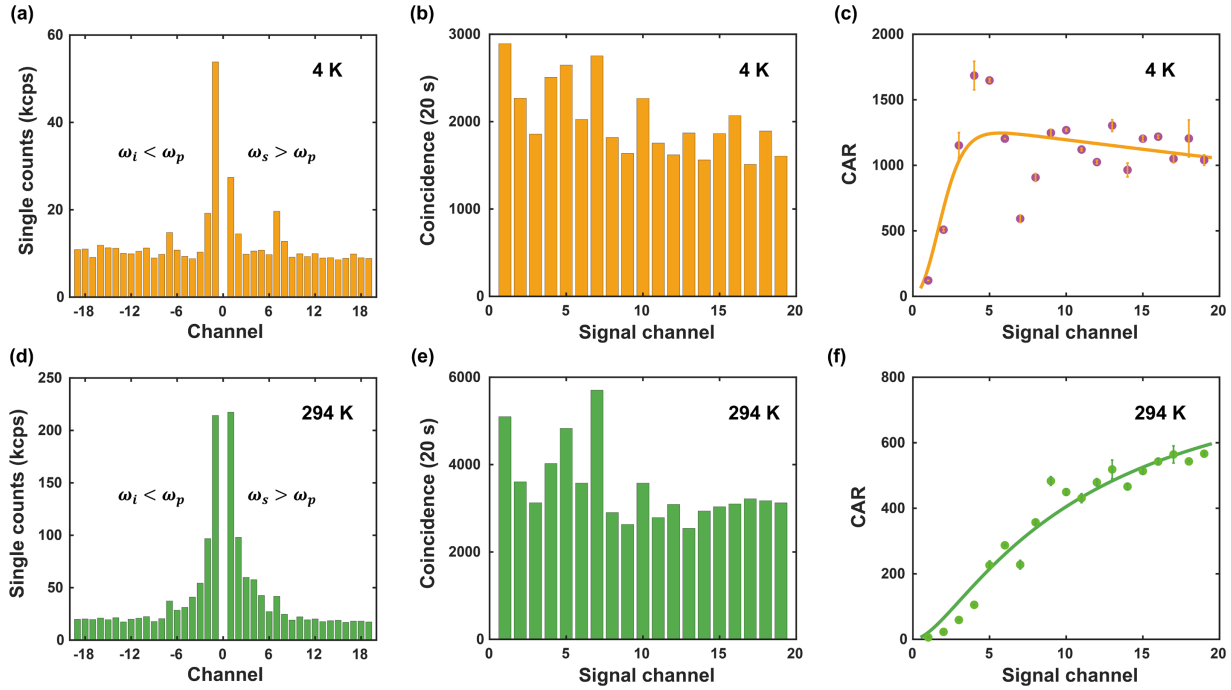

Fig. 2. Frequency-multiplexed photon-pair sources generated at cryogenic and room temperatures with a silicon photonics chip. (a) Continuous emission spectra at 4 K from the 40-channel DWDM system. The frequencies of the correlated photon pairs are equally separated from the central pump frequency. (b) Coincidence measurements in 20 s intervals of the photon pairs in different frequency channels at 4 K. (c) CAR values in different frequency channels at 4 K and the corresponding fitted curve. (d) Continuous emission spectra at 294 K. (e) Coincidence measurements of the photon pairs at 294 K. (f) CAR values in different frequency channels at 294 K and the corresponding fitted curve. All data are averages of two consecutive measurements, from which error bars of CAR values are given.

where G is the brightness of SFWM, $n_{s\,(i)}$ is the noise in the signal (idler) channels, $\eta_{s\,(i)}$ is the transmission and detection loss of the signal (idler) photons, and $D_{s\,(i)}$ is the dark count of the photon detectors. Because of the near-zero phase matching condition in SFWM [2], the source brightness G can be considered as frequency independent. If we neglect noise and the dark count of photon detectors, CAR has the form of $1/t_{\text{win}}G$. This is simply a frequency-independent flat line, and it naturally increases as the source brightness G decreases. However, noise is frequency dependent and changes the ideal pattern of CAR. The noise in the photonic source mainly includes spontaneous Raman scattering (SpRS) in the connected fiber and nonlinear scattering in the silicon waveguides [36]. By removing the silicon chip and connecting the fiber in the cryostat, we measured the fluorescence spectrum with the same experimental setting to characterize SpRS noise in the fiber, and the results are given in Supplement 1. We found that the unfiltered pump existed in only one channel closest to the pump, and this could not explain the higher scattering noise in Figs. 2(a) and 2(d) for channels close to the pump. It is temperature dependent and was explained as phonon-based inelastic light scattering in Ref. [36] and fundamental thermodynamic fluctuations in Ref. [37]. Our calculation using the phonon-based model [38–41] shows that there exists one small peak close to the pump in silicon waveguides, which may explain the source of the noise at small detuning. More details are given in Supplement 1.

We take one common channel, C43, as an example and estimate the proportion of noise generated in the silicon waveguide and fiber to the detected single-photon count at this channel. At room temperature, noise in the fiber and silicon waveguide accounts for 12% and 30%, respectively. At 4 K, the noise in the silicon waveguide was negligible, and the noise in the fiber accounts for 25% of the single-photon count. Because the fluorescence noise in the fiber is proportional to the fiber length, we can reduce the length of the fiber between filters to mitigate the influence of noise in the fiber.

By combining SFWM and SpRS, we fitted the CAR data. The CAR fitted curves for different temperatures are also given in Figs. 2(c) and 2(f). Considering that the dark count of single-photon detectors is much lower than the detected single-photon count, we neglected them in fitting for simplicity. The fitted source brightness at different temperatures is $G(4\,\text{K}) = 107\,\text{kHz}$ and $G(294\,\text{K}) = 1003\,\text{kHz}$, which are close to the theoretical estimation (see Supplement 1).

To better understand the properties of photonic sources at cryogenic temperatures, we chose correlated frequency channels ± 9 as an example and recorded the coincidence and CAR results with 2 mW pump and temperatures ranging from 4 to 294 K. The experimental results are shown in Figs. 3(a) and 3(b), and we can see that as the temperature rises, the brightness of the photon-pair source increases while the CAR decreases. The brightness of the source is proportional to the square of the Kerr nonlinear parameter, and the data can be fitted based on the empirical formula in Ref. [35]. It has the form of

$$C_{\text{exp}}(T) = C_{\text{exp}}(0)\left[\frac{1}{\exp(E_{\text{ph}}/k_B T) - 1} + \frac{1}{1 - \exp(-E_{\text{ph}}/k_B T)}\right]^2. \tag{2}$$

Here, the fitting parameters are the detected two-photon coincidence count at 0 K, $C_{\text{exp}}(0) = 1481$, and $E_{\text{ph}}/k_B = 614$ K. We fitted the CAR results using Eq. (1) with temperature-dependent source brightness [Eq. (2)]. Next, we consider the influence of pump power on the properties of quantum photonic sources.

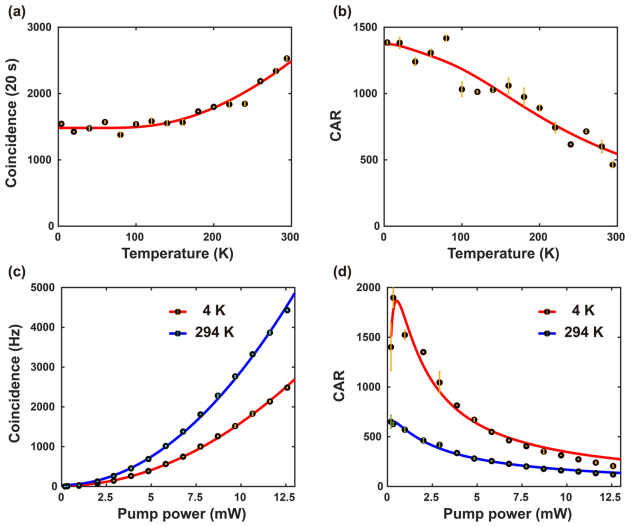

Fig. 3. Temperature and pump power dependence of the photon-pair source with correlated frequency channels ±9. (a) Temperature dependence of the source brightness and the fitted curve. (b) Temperature dependence of CAR and the fitted curve. (c) Two-photon coincidence results as a function of the input pump power at 4 and 294 K. The data were obtained with different integration times and normalized according to the integration time. (d) CAR values as a function of the input pump power at 4 and 294 K.

By changing the input pump power, we measured the two-photon coincidence and CAR results as a function of the pump power at temperatures of 4 and 294 K, respectively. The results are shown in Figs. 3(c) and 3(d). We find that for both quantum photonic sources at different temperatures, the two-photon coincidence values show a quadratic function of the pump power, and CAR values can be well fitted with Eq. (1). Compared to the results at room temperature, CAR values at cryogenic conditions achieve a nearly two-fold improvement, even at the extreme power of the experiment. Considering that the photonic source at different temperatures has the same brightness, such as 1800 Hz, CAR at 4 K still achieves a 1.35-fold increase over that at room temperature because of noise suppression caused by cryogenic cooling. Noise suppression predicts the improvement of single-photon purity, and second-order correlation measurements [28] with 4 mW pump show that the $g^{(2)}(0)$ value is reduced from 0.055 ± 0.007 at room temperature to 0.035 ± 0.005 at 4 K.

In many cases, such as multi-photon applications, the photonic sources with the pulsed laser pump are always used, which show lower noise than that with the CW laser pump. With 160 μW picosecond pulsed laser pump power [2], we also recorded the coincidence and CAR results at different temperatures. The results are shown in Fig. 4, and coincidence values show a similar pattern as in the CW laser pump. Although the improvement is not as pronounced as in the case of the CW pump, the CAR value is also improved at lower temperatures.

C. Entanglement Generation and Verification

This cryogenic integrated photon-pair source has many applications, one of which is to generate quantum entangled states, which lies at the heart of quantum information studies. Here, we used one common UMI to generate energy–time entanglement, which is widely used for quantum information processing, such as quantum cryptography [42] and Bell-type tests [43]. The UMI

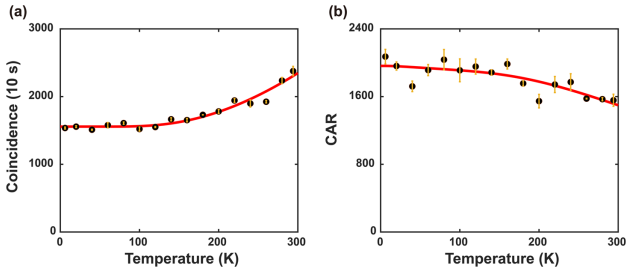

Fig. 4. Temperature dependence of the photon-pair source's (a) brightness and (b) CAR with pulsed laser pump.

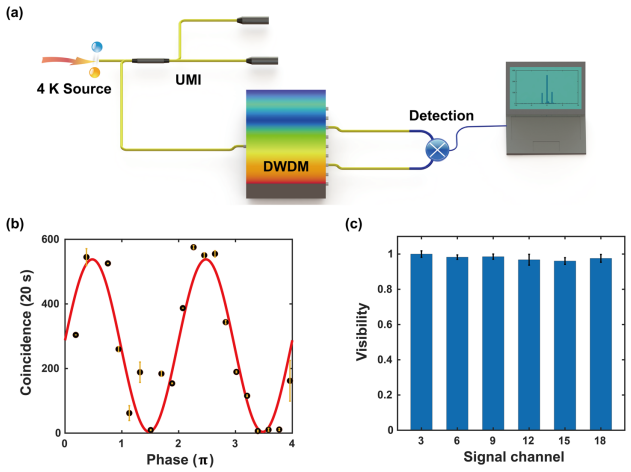

Fig. 5. Energy–time entanglement interference measurements. (a) Experimental setup for entanglement generation and detection. (b) Coincidence results as a function of the total UMI phase for photon-pair source with frequency channels ±9. (c) Interference visibility for six correlated channels. UMI, unbalanced Michelson interferometer; DWDM, dense-wave-division multiplexer.

consists of one 50/50 beam splitter, two Faraday mirrors, and the connected optical fiber. In the experiment, the signal and idler photons generated by the silicon nanowire at 4 K were first input into the UMI and then separated by the DWDM for further detection and analysis [Fig. 5(a)]. By post-selection of the central peak of the coincidences with a 0.4 ns time window, we obtained the energy–time entangled state in the form of

$$|\psi\rangle = \frac{1}{\sqrt{2}}(|L\rangle|L\rangle + e^{i\varphi}|S\rangle|S\rangle), \tag{3}$$

where φ is the phase difference obtained by both the signal and idler photons over the short (S) arm and long (L) arm of the UMI. In the experiment, we sealed the UMI in one temperature control module and achieved phase modulation by changing the temperature [44]. To characterize the quality of the energy–time entangled state, we first recorded the two-photon interference fringe for the photon-pair source with frequency channels ±9. The coincidence counts in 20 s intervals are shown in Fig. 5(b) and vary sinusoidally with the UMI phase. The fitted interference fringe with a function of $1 + V\sin[\pi(\varphi - \varphi_c)/T]$ has a raw visibility of 0.985 ± 0.015, where V is the fringe visibility, φ_c is the initial phase, and T is the oscillation period. In the test, we observed very low accidental coincidence noise (around 1 Hz in 20 s intervals), which ensures high interference visibility. Moreover, the entangled photon-pair source is frequency multiplexed. We measured six correlated frequency channels, from ±3 to ±18, for quantification [Fig. 5(c)].

The raw visibilities are all around 0.98, and the high quality of this multichannel entangled source is ready for further quantum information applications.

3. DISCUSSION AND CONCLUSION

Our work experimentally confirms that even under cryogenic conditions, SFWM in silicon waveguides is still an efficient method for generating quantum photonic sources. Cryogenic cooling suppresses noise, and a high-quality quantum photonic source is achieved. Combined with cryogenic integrated photonic modulators [45,46], a variety of photonic quantum applications can be performed using QPICs under cryogenic operation conditions. In particular, SNSPDs with excellent performance also operate at similar temperatures. Integrated photonic devices that contain all core functions, such as photonic source generation, quantum state modulation, and single-photon detection, will greatly reduce chip-in and chip-out losses, thus promoting photonic quantum applications in daily life. For fully integrated operation, pump filtering at cryogenic temperatures is also very important, and verifying its functions will be the next step. Beyond the quantum photon-pair source, our work will promote other cryogenic nonlinear applications such as all-optical modulation, wavelength conversion, and parametric amplification with silicon photonic circuits.

In conclusion, we demonstrate quantum photon-pair source preparation with integrated silicon photonic circuits under cryogenic conditions. It has been proven that SFWM in silicon waveguides is still an efficient method for generating quantum photonic sources at this low temperature. Photon pairs are experimentally verified with a bandwidth of ∼2 THz, and frequency-multiplexed energy–time entangled states are generated. The observed near-unity interference visibility indicates that this cryogenic multichannel entangled photonic source has high quality and is ready for further quantum information applications. Our work is an important part of cryogenic nonlinear photonics and will be further used for scalable quantum information applications.

Funding. Innovation Program for Quantum Science and Technology (2021ZD0301500, 2021ZD0303200); National Natural Science Foundation of China (12004373, 62061160487, 62275240); Key Research and Development Program of Anhui Province (2022b1302007); China Postdoctoral Science Foundation (2021T140647); Fundamental Research Funds for the Central Universities.

Acknowledgment. We thank Chen-Wei Chen for useful suggestions on revising the language of this article. This work was partially carried out at the USTC Center for Micro and Nanoscale Research and Fabrication.

Disclosures. The authors declare no conflicts of interest.

Data availability. Data underlying the results presented in this paper are not publicly available at this time but may be obtained from the authors upon reasonable request.

Supplemental document. See Supplement 1 for supporting content.

REFERENCES

1. J. Wang, F. Sciarrino, A. Laing, and M. G. Thompson, "Integrated photonic quantum technologies," Nat. Photonics **14**, 273–284 (2020).
2. M. Zhang, L. T. Feng, Z. Y. Zhou, Y. Chen, H. Wu, M. Li, S. M. Gao, G. P. Guo, G. C. Guo, D. X. Dai, and X. F. Ren, "Generation of multiphoton quantum states on silicon," Light Sci. Appl. **8**, 41 (2019).
3. L. T. Feng, G. C. Guo, and X. F. Ren, "Progress on integrated quantum photonic sources with silicon," Adv. Quantum Technol. **3**, 1900058 (2020).
4. S. Paesani, M. Borghi, S. Signorini, A. Maïnos, L. Pavesi, and A. Laing, "Near-ideal spontaneous photon sources in silicon quantum photonics," Nat. Commun. **11**, 2505 (2020).
5. V. D. Vaidya, B. Morrison, L. G. Helt, R. Shahrokshahi, D. H. Mahler, M. J. Collins, K. Tan, J. Lavoie, A. Repingon, M. Menotti, N. Quesada, R. C. Pooser, A. E. Lita, T. Gerrits, S. W. Nam, and Z. Vernon, "Broadband quadrature-squeezed vacuum and nonclassical photon number correlations from a nanophotonic device," Sci. Adv. **6**, eaba9186 (2020).
6. J. Carolan, C. Harrold, C. Sparrow, E. Martin-López, N. J. Russell, J. W. Silverstone, P. J. Shadbolt, N. Matsuda, M. Oguma, M. Itoh, G. D. Marshall, M. G. Thompson, J. C. F. Matthews, T. Hashimoto, J. L. O'Brien, and A. Laing, "Universal linear optics," Science **349**, 711–716 (2015).
7. N. C. Harris, G. R. Steinbrecher, M. Prabhu, Y. Lahini, J. Mower, D. Bunandar, C. Chen, F. N. C. Wong, T. Baehr-Jones, M. Hochberg, S. Lloyd, and D. Englund, "Quantum transport simulations in a programmable nanophotonic processor," Nat. Photonics **11**, 447–452 (2017).
8. C. Sparrow, E. Martín-López, N. Maraviglia, A. Neville, C. Harrold, J. Carolan, Y. N. Joglekar, T. Hashimoto, N. Matsuda, J. L. O'Brien, D. P. Tew, and A. Laing, "Simulating the vibrational quantum dynamics of molecules using photonics," Nature **557**, 660–667 (2018).
9. X. Qiang, X. Zhou, J. Wang, C. M. Wilkes, T. Loke, S. O'Gara, L. Kling, G. D. Marshall, R. Santagati, T. C. Ralph, J. B. Wang, J. L. O'Brien, M. G. Thompson, and J. C. F. Matthews, "Large-scale silicon quantum photonics implementing arbitrary two-qubit processing," Nat. Photon. **12**, 534–539 (2018).
10. C. Taballione, R. van der Meer, H. J. Snijders, P. Hooijschuur, J. P. Epping, M. de Goede, B. Kassenberg, P. Venderbosch, C. Toebes, H. van den Vlekkert, P. W. H. Pinkse, and J. J. Renema, "A universal fully reconfigurable 12-mode quantum photonic processor," Mater. Quantum Technol. **1**, 035002 (2021).
11. J. M. Arrazola, V. Bergholm, K. Brádler, T. R. Bromley, M. J. Collins, I. Dhand, A. Fumagalli, T. Gerrits, A. Goussev, L. G. Helt, and J. Hundal, "Quantum circuits with many photons on a programmable nanophotonic chip," Nature **591**, 54–60 (2021).
12. W. H. P. Pernice, C. Schuck, O. Minaeva, M. Li, G. N. Goltsman, A. V. Sergienko, and H. X. Tang, "High-speed and high-efficiency travelling wave single-photon detectors embedded in nanophotonic circuits," Nat. Commun. **3**, 1325 (2012).
13. F. Najafi, J. Mower, N. C. Harris, F. Bellei, A. Dane, C. Lee, X. Hu, P. Kharel, F. Marsili, S. Assefa, K. K. Berggren, and D. Englund, "On-chip detection of non-classical light by scalable integration of single-photon detectors," Nat. Commun. **6**, 5873 (2015).
14. P. Vines, K. Kuzmenko, J. Kirdoda, D. C. S. Dumas, M. M. Mirza, R. W. Millar, D. J. Paul, and G. S. Buller, "High performance planar germanium-on-silicon single-photon avalanche diode detectors," Nat. Commun. **10**, 1086 (2019).
15. A. Reiserer and G. Rempe, "Cavity-based quantum networks with single atoms and optical photons," Rev. Mod. Phys. **87**, 1379 (2015).
16. A. W. Elshaari, W. Pernice, K. Srinivasan, O. Benson, and V. Zwiller, "Hybrid integrated quantum photonic circuits," Nat. Photon. **14**, 285–298 (2020).
17. X. Zhang, H. O. Li, G. Cao, M. Xiao, G. C. Guo, and G. P. Guo, "Semiconductor quantum computation," Natl. Sci. Rev. **6**, 32–54 (2019).
18. A. O. Niskanen, K. Harrabi, F. Yoshihara, Y. Nakamura, S. Lloyd, and J. S. Tsai, "Quantum coherent tunable coupling of superconducting qubits," Science **316**, 723–726 (2007).
19. N. A. Lange, J. P. Höpker, R. Ricken, V. Quiring, C. Eigner, C. Silberhorn, and T. J. Bartley, "Cryogenic integrated spontaneous parametric down-conversion," Optica **9**, 108–111 (2022).
20. L. Feng, M. Zhang, J. Wang, X. Zhou, X. Qiang, G. Guo, and X. Ren, "Silicon photonic devices for scalable quantum information applications," Photon. Res. **10**, A135–A153 (2022).
21. M. A. Foster, A. C. Turner, J. E. Sharping, B. S. Schmidt, M. Lipson, and A. L. Gaeta, "Broad-band optical parametric gain on a silicon photonic chip," Nature **441**, 960–963 (2006).
22. X. Liu, R. M. Osgood, Y. A. Vlasov, and W. M. Green, "Mid-infrared optical parametric amplifier using silicon nanophotonic waveguides," Nat. Photonics **4**, 557–560 (2010).

23. A. Pasquazi, Y. Park, J. Azaña, F. Légaré, R. Morandotti, B. E. Little, S. T. Chu, and D. J. Moss, "Efficient wavelength conversion and net parametric gain via four wave mixing in a high index doped silica waveguide," Opt. Express **18**, 7634–7641 (2010).
24. M. J. Collins, C. Xiong, I. H. Rey, T. D. Vo, J. He, S. Shahnia, C. Reardon, T. F. Krauss, M. J. Steel, A. S. Clark, and B. J. Eggleton, "Integrated spatial multiplexing of heralded single-photon sources," Nat. Commun. **4**, 2582 (2013).
25. C. Reimer, L. Caspani, M. Clerici, M. Ferrera, M. Kues, M. Peccianti, A. Pasquazi, L. Razzari, B. E. Little, S. T. Chu, D. J. Moss, and R. Morandotti, "Integrated frequency comb source of heralded single photons," Opt. Express **22**, 6535–6546 (2014).
26. C. Xiong, X. Zhang, Z. Liu, M. J. Collins, A. Mahendra, L. G. Helt, M. J. Steel, D.-Y. Choi, C. J. Chae, P. H. W. Leong, and B. J. Eggleton, "Active temporal multiplexing of indistinguishable heralded single photons," Nat. Commun. **7**, 10853 (2016).
27. J. Wang, S. Paesani, Y. Ding, R. Santagati, P. Skrzypczyk, A. Salavrakos, J. Tura, R. Augusiak, L. Mančinska, D. Bacco, D. Bonneau, J. W. Silverstone, Q. Gong, A. Acín, K. Rottwitt, L. K. Oxenløwe, J. L. O'Brien, A. Laing, and M. G. Thompson, "Multidimensional quantum entanglement with large-scale integrated optics," Science **360**, 285–291 (2018).
28. L. T. Feng, M. Zhang, X. Xiong, Y. Chen, H. Wu, M. Li, G. P. Guo, G. C. Guo, D. X. Dai, and X. F. Ren, "On-chip transverse-mode entangled photon pair source," npj Quantum Inf. **5**, 2 (2019).
29. X. Lu, Q. Li, D. A. Westly, G. Moille, A. Singh, V. Anant, and K. Srinivasan, "Chip-integrated visible-telecom entangled photon pair source for quantum communication," Nat. Phys. **15**, 373–381 (2019).
30. L. T. Feng, M. Zhang, Z. Y. Zhou, Y. Chen, M. Li, D. X. Dai, H. L. Ren, G. P. Guo, G. C. Guo, M. Tame, and X. F. Ren, "Generation of a frequency-degenerate four-photon entangled state using a silicon nanowire," npj Quantum Inf. **5**, 90 (2019).
31. J. C. Adcock, C. Vigliar, R. Santagati, J. W. Silverstone, and M. G. Thompson, "Programmable four-photon graph states on a silicon chip," Nat. Commun. **10**, 3528 (2019).
32. D. Llewellyn, Y. Ding, I. I. Faruque, S. Paesani, D. Bacco, R. Santagati, Y. J. Qian, Y. Li, Y. F. Xiao, M. Huber, and M. Malik, "Chip-to-chip quantum teleportation and multi-photon entanglement in silicon," Nat. Phys. **16**, 148–153 (2020).
33. Y. Zhao, Y. Okawachi, J. K. Jang, X. Ji, M. Lipson, and A. L. Gaeta, "Near-degenerate quadrature-squeezed vacuum generation on a silicon-nitride chip," Phys. Rev. Lett. **124**, 193601 (2020).
34. Z. Yang, M. Jahanbozorgi, D. Jeong, S. Sun, O. Pfister, H. Lee, and X. Yi, "A squeezed quantum microcomb on a chip," Nat. Commun. **12**, 4781 (2021).
35. G. F. Sinclair, N. A. Tyler, D. Sahin, J. Barreto, and M. G. Thompson, "Temperature dependence of the Kerr nonlinearity and two-photon absorption in a silicon waveguide at 1.55 μm," Phys. Rev. Appl. **11**, 044084 (2019).
36. S. Clemmen, A. Perret, J. Safioui, W. Bogaerts, R. Baets, S.-P. Gorza, P. Emplit, and S. Massar, "Low-power inelastic light scattering at small detunings in silicon wire waveguides at telecom wavelengths," J. Opt. Soc. Am. B **29**, 1977–1982 (2012).
37. N. L. Thomas, A. Dhakal, A. Raza, F. Peyskens, and R. Baets, "Impact of fundamental thermodynamic fluctuations on light propagating in photonic waveguides made of amorphous materials," Optica **5**, 328–336 (2018).
38. D. Dimitropoulos, V. Raghunathan, R. Claps, and B. Jalali, "Phase-matching and nonlinear optical processes in silicon waveguides," Opt. Express **12**, 149–160 (2004).
39. Q. Lin and G. P. Agrawal, "Silicon waveguides for creating quantum-correlated photon pairs," Opt. Lett. **31**, 3140–3142 (2006).
40. Q. Lin, O. J. Painter, and G. P. Agrawal, "Nonlinear optical phenomena in silicon waveguides: Modeling and applications," Opt. Express **15**, 16604–16644 (2007).
41. K. Harada, H. Takesue, H. Fukuda, T. Tsuchizawa, T. Watanabe, K. Yamada, Y. Tokura, and S. Itabashi, "Frequency and polarization characteristics of correlated photon-pair generation using a silicon wire waveguide," IEEE J. Sel. Top. Quantum Electron. **16**, 325–331 (2010).
42. W. Tittel, J. Brendel, H. Zbinden, and N. Gisin, "Quantum cryptography using entangled photons in energy-time Bell states," Phys. Rev. Lett. **84**, 4737 (2000).
43. R. T. Thew, A. Acín, H. Zbinden, and N. Gisin, "Bell-type test of energy-time entangled qutrits," Phys. Rev. Lett. **93**, 010503 (2004).
44. Y. H. Li, Z. Y. Zhou, L. T. Feng, W. T. Fang, S. L. Liu, S. K. Liu, K. Wang, X. F. Ren, D. S. Ding, L. X. Xu, and B. S. Shi, "On-Chip multiplexed multiple entanglement sources in a single silicon nanowire," Phys. Rev. Appl. **7**, 064005 (2017).
45. U. Chakraborty, J. Carolan, G. Clark, D. Bunandar, G. Gilbert, J. Notaros, M. R. Watts, and D. R. Englund, "Cryogenic operation of silicon photonic modulators based on the DC Kerr effect," Optica **7**, 1385–1390 (2020).
46. M. Dong, G. Clark, A. J. Leenheer, M. Zimmermann, D. Dominguez, A. J. Menssen, D. Heim, G. Gilbert, D. Englund, and M. Eichenfield, "High-speed programmable photonic circuits in a cryogenically compatible, visible–near-infrared 200 mm CMOS architecture," Nat. Photonics **16**, 59–65 (2022).